

https://dspace.org/

Random sampling-based relative radiometric normalisation

Bonnet, Wessel

2021
https://hdl.handle.net/10539/33043

Downloaded from a DSpace repository. https://dspace.org/

Random Sampling-based Relative Radiometric Normalisation

Wessel Bonnet

Supervisor(s):
Turgay Çelik



A research report submitted in partial fulfillment of the requirements for the degree of Master of Science in the field of e-Science

in the

School of Computer Science and Applied Mathematics
University of the Witwatersrand, Johannesburg

8 October 2021

Declaration

I, Wessel Bonnet, declare that this research report is my own, unaided work. It is being submitted for the degree of Master of Science in the field of e-Science at the University of the Witwatersrand, Johannesburg. It has not been submitted for any degree or examination at any other university.

Portions of this work have been submitted for publication as "W. Bonnet and T. Celik, "Random Sampling-Based Relative Radiometric Normalization", in *IEEE Geoscience and Remote Sensing Letters*, doi: 10.1109/LGRS.2020.3047344.".



Wessel Bonnet

8 October 2021

Abstract

Relative radiometric normalisation (RRN) is a widely used methodology for change detection and radiometric calibration of corresponding multispectral images for further analysis. However, standard RRN methods are not robust against anomalous (or outlier) pixels, which warp the calibration and decrease the spectral similarity of processed images. This research seeks to improve the calibration of corresponding multispectral images through relative radiometric normalisation by utilising a novel random sampling-based method based on the random sampling consensus (RANSAC) to exclude outlier pixels from the analysis. A comparison is made against the widely used Covariance Equalisation (CE), Multivariate Alteration Detection (MAD), Iteratively Reweighted MAD (IR-MAD) and Iterative Slow Feature Analysis (ISFA) algorithms in terms of computing times, mean squared error and the structural similarity index measure. The experimental results show that the proposed method performs favourably against CE, MAD, IR-MAD and ISFA in all metrics considered in this research.

Acknowledgements

Firstly, my gratitude goes out to my supervisor for his academic input and support, for providing a good topic for research, and for his patience.
Secondly, I would like to acknowledge the broader School of Computer Science and Applied Mathematics e-Science collective for their assistance, including the internal review.
This research was funded by the DSI-NICIS National e-Science Postgraduate Teaching and Training Platform.

Contents

Declaration i

Abstract ii

Acknowledgements iii

List of Tables vi

1 Introduction 1
- 1.1 Background . . . 1
  - 1.1.1 Research Area . . . 1
  - 1.1.2 Research Problem . . . 1
  - 1.1.3 Contextualisation . . . 2
- 1.2 Problem Statement . . . 5
- 1.3 Research Aims and Objectives . . . 6
  - 1.3.1 Research Aim . . . 6
  - 1.3.2 Research Objectives . . . 6
  - 1.3.3 Research Context and Contribution . . . 7
- 1.4 Overview . . . 7
- 1.5 Delineations, Limitations, and Assumptions . . . 8

2 Literature Review 9
- 2.1 Relative Radiometric Normalisation . . . 9
- 2.2 Regression RRN . . . 10
- 2.3 Covariance Equalisation . . . 10
- 2.4 Multivariate Alteration Detection . . . 11
- 2.5 Iteratively Reweighted Multivariate Alteration Detection . . . 12
- 2.6 Iterative Slow Feature Analysis . . . 12
- 2.7 RANSAC and related methods . . . 13

2.8 Structural Similarity Index Measure 14

3 Research Methodology **16**
3.1 Research design 16
3.2 Data 17
3.3 Proposed method 19
3.3.1 Random Sampling-based RRN (RS-RRN) 19
3.3.2 Weighted RS-RRN 22
3.3.3 SLIC RS-RRN 22
3.4 Analysis 23
3.5 Parameter Optimisation 24

4 Results and Discussion **26**
4.1 Quantitative comparisons 26
4.1.1 Comparison of RS-RRN algorithms 26
4.2 Qualitative comparisons 30
4.3 Other RANSAC-based algorithms 33
4.4 Summary 34

5 Conclusions and Future Work **35**
5.1 Conclusions 35
5.2 Future Work 36

Bibliography **37**

List of Tables

3.1 Optimised parameters for the spectral calibration methodologies . . 24

4.1 SSIM comparisons of 100 trials of RS-RRN methods 27
4.2 MSE comparisons of 100 trials of RS-RRN methods 27
4.3 PSNR comparisons of 100 trials of RS-RRN methods 27
4.4 Time comparisons of 100 trials of RS-RRN methods 28
4.5 Comparison against other RRN methods 29

Chapter 1

Introduction

1.1 Background

1.1.1 Research Area

The research falls within the subject areas of image processing, computer vision and remote sensing, and utilises methodologies from machine learning and statistics. More specifically, the research deals with the Relative Radiometric Normalisation (RRN) of geometrically calibrated images, and leverages sampling techniques based on the Random Sampling Consensus (RANSAC).

1.1.2 Research Problem

Relative radiometric normalisation (RRN) is widely used as a method to spectrally align images of the same area at different time points. In order to calibrate any pair of images, spectral adjustments are performed on one of the images (called the subject image), to more closely align to the other image (called the reference image). This is required, since corresponding images are captured under very different weather conditions, times of day or image capturing configurations. They may also be captured using entirely different equipment.

More specifically, spectral band values at the same point could have vastly different readings at different time points, but still contain the same physical object or land cover category. This can create confusion or skewing within spectral readings, which is especially detrimental if objects or land cover classes need to be analysed based on spectral signatures. This justifies the use of relative radiometric normalisation to correct the overall spectral readings or colours.

Images can be normalised to correspond in their entirety by standard RRN correction. However, spectral discrepancies brought about by individually anomalous pixels are not accounted for. This is because RRN is performed on the full images. Anomalies can be brought about for a number of reasons, including cloud or snow cover, highly reflective areas or digital errors. Anomalous pixels need to be removed from the broader analysis due to their high-leverage and outliership in normalisation models, and undue impact on the normalisation of the spectral readings. Currently used algorithms for the removal of anomalous pixels are very sensitive to parameter inputs, do not always yield good results, or are computationally expensive.

This research proposes to leverage a random sampling methodology based on RANSAC, which provides a robust methodology through which images with spatial discrepancies can be calibrated in terms of their matching pixel geometries or signatures. Since its underlying methodology requires only a linear regression model and a specified performance metric in its detection and inclusion of inlier pixels, random sampling and its related methodologies can easily be applied to radiometric calibration as well, and it is expected to provide a more robust framework under which to perform relative radiometric normalisation in the presence of spectral anomalies.

1.1.3 Contextualisation

Relative radiometric normalisation was first developed by Schott, Salvaggio, and Volchok [16], and has become a widely used methodology to calibrate co-registered images by minimising inherent radiometric discrepancies caused by various inconsistencies of the acquisition conditions. Relative radiometric normalisation seeks to find the set of parameters to radiometrically align subject and reference image through the use of a linear regression model between the pixels of the reference and subject images. The model can utilise either all pixels of reference and subject images or a subset of it to estimate the linear model parameters.

Since several anomalous or changed pixels are commonly found in corresponding image pairs, and RRN analysis is warped by these pixels, Covariance Equalisation (CE), proposed by Schaum and Stocker [15] was developed to filter out

these changed pixels. In the CE methodology, inter-band covariances in the subject and reference images are decomposed and covariances are matched to better detect anomalies for exclusion.

The Multivariate Alteration Detection (MAD) algorithm developed by Nielsen, Conradsen, and Simpson [11] is another such extension to RRN, where inconsistent or anomalous pixels are excluded from analysis. Multispectral images are made to correspond between two time points by performing canonical correlation analysis to find the pixels displaying the largest amount of variation within each of the spectral bands within the difference image [25].

The Iteratively Reweighted MAD (IR-MAD) algorithm developed by Nielsen [10] extended the MAD methodology by iteratively alternating between the MAD process and the reweighting of pixels to assign higher weights to observations that do not show large changes over time, and lower weights to changed pixels which represent spectral anomalies.

The Iterative Slow Feature Analysis (ISFA) algorithm proposed by Zhang, Wu, and Du [24] provides a similar iterative reweighting scheme to more clearly separate changed and unchanged pixels by extracting their invariant features through a slow feature analysis transformation, and progressively assigning larger weights to pixels showing good correspondence between the subject and reference images.

This research will leverage a random sampling-based methodology based on the principles and methods of the random sample consensus (RANSAC) algorithm developed by Fischler and Bolles [5] to find a suitable sample of pixels with which to calibrate corresponding images. RANSAC has become one of the most popular robust estimators within the computer vision field. Its implementation is performed through randomly selecting subsets of pixels from input images, and computing parameters to fit models to these samples. This methodology has been utilised in several different contexts, especially within robust uncalibrated image matching applications, which include short-baseline stereo applications [17], [18] and wide-baseline stereo applications [12], [14], [19], mosaicing [9], motion segmentation [17], eigenimage matching [7], geometric primitives detection [4] and many other applications.

RANSAC has seen a number of variations and extensions since its original conception. Chum, Matas, and Kittler [3] developed an algorithm for Locally Optimized (LO) RANSAC, which utilises the result that any model fitted from uncontaminated minimal samples very likely has a substantial proportion of inliers in its support. Within the LO-RANSAC framework, an optimisation step is added to the standard RANSAC algorithm, with the standard algorithm's best solution used as the initial point for the optimisation. Non-minimal samples are created from the inlier set identified by the RANSAC algorithm, and more robust regression models are fitted to these larger samples.

Chum and Matas [2] updated the RANSAC algorithm to develop the PROSAC method, which measures the quality of data sampled within the RANSAC algorithm, and preferentially selecting data subsets which are more likely to generate valid model. Subsets are no longer selected randomly, but are rather selected from progressively growing sets of the highest-ranking element correspondences.

Matas and Chum [8] developed the R-RANSAC with a sequential probability ratio test method that finds, like RANSAC, a solution that is optimal with a specified probability, and provides an optimal verification strategy based on Wald's theory of sequential decision making [20] for the case where data outlier contamination levels are known. This method is shown to greatly improve computational speed and outlier identification.

Raguram et al. [13] consolidates the RANSAC and RANSAC-based robust estimation methods to provide a comprehensive analysis and comparison between the different approaches above. In addition to this, a consolidated framework called the Universal Random Sample Consensus (USAC) is formulated which serves as a generalisation of all the different RANSAC-based frameworks and can be customised to align to any of the RANSAC-based methods. This framework allows for a much greater degree of flexibility and customisation compared to the random hypothesis generation and verification structure used in the standard RANSAC method by incorporating the computational and practical modifications developed in the more recent RANSAC-based algorithms.

The structural similarity index measure (SSIM) was first proposed by Wang et al. [21], and was developed as a metric to measure the similarity between images. This provides a valuable tool to analyse the quality of calibrations between image pairs under each of the change detection algorithms.

Deep learning-based methods have also been explored by various authors conducting research in this area. Gong et al. [6] developed a method to detect invariant features by developing a deep neural network, and thereby produce a change map from two corresponding images using the pretrained neural network. Deep feature learning has also been utilised in conjunction with the ISFA algorithm by Xu et al. [22], for use in change detection within high-resolution remote sensing images.

Lastly, nonlinear relative radiometric normalisation has also been adressed in the literature. Yin et al. [23] put forward a nonlinear radiometric normalisation model for Satellite Image Time Series built on Artificial Neural Networks (ANN) and a Greedy Algorithm (GA), where linear RRN models are unable to account for nonlinear changes aggregating over multiple time lapses.

1.2 Problem Statement

Relative radiometric normalisation is a widely used methodology to spectrally calibrate corresponding multispectral images for further analysis. More specifically, it minimises the inherent radiometric discrepancies caused by illumination differences, atmospheric variations and sensor response settings. However, standard RRN is not robust against anomalous pixels, high-leverage, outlier readings, whch unduly warp the calibration and decrease the spectral similarity of the processed images.

Existing covariance analysis-based algorithms such as Covariance Equalisation (CE) and the Multivariate Alteration Detection (MAD) algorithms do not always yield improved calibration accuracy, whereas iterative approaches such as the Iteratively Reweighted Multivariate Alteration Detection (IR-MAD) and the Iterative Slow Feature Analysis (ISFA) are sometimes computationally expensive. In addition to these factors, all currently used algorithms are very sensitive to parameter inputs, and require careful pre-calibration before use.

This research seeks to explore whether the relative radiometric normalisation of corresponding images could be improved by utilising a random sampling-based method leveraging RANSAC methodologies to exclude outlier pixels from the analysis by demonstrating higher calibration accuracies or lower computational times.

1.3 Research Aims and Objectives

1.3.1 Research Aim

The research focuses on the description, implementation, use, and testing of a novel random sampling method for the radiometric calibration of geometrically co-registered multiband images.

The proposed Random Sampling based RRN method is compared to regression RRN, Covariance Equalisation, Multivariate Alteration Detection, Iteratively Reweighted Multivariate Alteration Detection and the Iterative Slow Feature Analysis algorithms for a set of coregistered image pairs in terms of visual similarities, running times, mean squared error (MSE), peak signal-to-noise ratio (PSNR) and the structural similarity index measure (SSIM).

It is hypothesised that the similarity scores of multispectral images aligned using RRN will be improved by utilising RANSAC and related methods to exclude outlier pixels from the analysis. This will improve the extent to which geometrically calibrated image pairs can be radiometrically calibrated in the presence of anomalous pixels.

1.3.2 Research Objectives

The above aim of this research project is achieved through the following objectives (goals):

- To develop a novel radiometric normalisation algorithm leveraging a random sampling mechanism to align multispectral images captured at two time points.
- To develop a mechanism to adaptively calibrate the parameters of the developed algorithm to achieve improved computational and spectral correspondence results.
- To compare the developed random sampling algorithm to the Covariance Equalisation (CE) [15], Multivariate Alteration Detection (MAD) [11], Iteratively Reweighted MAD [10] and Iterative Slow Feature Analysis (ISFA) [24] algorithms in terms of running times, performance and yielded spectral similarities.

- To compare the visual results yielded by the random sampling RRN with those of the Covariance Equalisation (CE), Multivariate Alteration Detection (MAD), Iteratively Reweighted MAD (IR-MAD) and the Iterative Slow Feature Analysis (ISFA) algorithms in terms of visual correspondence between corrected images.

1.3.3 Research Context and Contribution

This research seeks to contribute to the body of knowledge regarding the radiometric calibration of geometrically co-registered multispectral images by describing a novel method to eliminate anomalous or outlier pixels to find a control set of inlier pixels with which to spectrally calibrate the images under analysis. The proposed method makes use of random sampling with methodologies loosely based on the random sampling consensus (RANSAC). This new method seeks to provide a favourable alternative to existing state-of-the-art inlier pixel subset selection strategies for Relative Radiometric Normalisation, such as the Iteratively Reweighted Multivariate Alteration Detection (IR-MAD) algorithm and the Iterative Slow Feature Analysis (ISFA) algorithm. Its tractability is predicated on improved image calibration metrics such as the Structural Similarity Index Measure (SSIM) and the Peak signal-to-noise ratio (PSNR), together with decreased computation times relative to existing methods.

1.4 Overview

The research is organised as follows:

- Chapter 1 provides an introduction and justification in terms of the context, related work and the aims and objectives of the research.
- Chapter 2 provides a more detailed literature review and a description of existing methods to provide further context for the research.
- Chapter 3 provides the methodology for the proposed algorithm as well as for alternative algorithms, details the experimental design and the image sets used to compare each of the algorithms, and provides the optimised parameters for each of the image pairs and algorithms.

- Chapter 4 discusses the results for each image pair for each of the algorithms, and provides analytical and qualitative comparisons between each of the algorithms.
- Chapter 5 concludes the research and proposes ideas for extensions to the research.

1.5 Delineations, Limitations, and Assumptions

In terms of the multispectral data being used, analysis is limited to actual multispectral images to demonstrate the tractability of the methods for practical data, although this also means that anomalous or error pixels are not known beforehand. For this reason, an accuracy test in terms of the identification of known outlier pixels and supervised machine learning falls out of the scope of the proposed research.

The research will focus on the radiometric calibration of co-registered (geometrically pre-calibrated) images with the same spatial resolution covering exactly the same area at different time points. Radiometric calibration of images with different resolutions or images covering differing but overlapping areas is not considered.

Deep learning approaches to Relative Radiometric Normalisation, kernel-based normalisation or any other nonlinear normalisation methods also fall out of the scope of this research.

Chapter 2

Literature Review

2.1 Relative Radiometric Normalisation

Relative radiometric normalization (RRN) is a spectral calibration method based on the pixel readings of geometrically aligned (or co-registered) images, whereby the images to be calibrated are set onto a common scale without any additional parameters or readings obtained from other measurements. Common features, landmarks or terrain contained in both images, referred to as invariant or unchanged features, can be leveraged to spectrally manipulate the images to appear as if they were captured by the same equipment under the same atmospheric conditions and photographic calibrations.

More specifically, for a given pair of geometrically aligned bitemporal multiband images S and R, with unchanged features consisting of pairs of geometrically corresponding pixels $\mathbf{S} \in S$ and $\mathbf{R} \in R$, RRN seeks to find a function f which minimises the distance $||f(\mathbf{S}) - \mathbf{R}||$. S is known as the subject image, since it is the image upon which the function f is performed. R is known as the reference image, since it is the image the function f seeks to align to. Relative radiometric calibration normalises the subject image by transforming its radiometric levels to let its features match as closely as possible to those of the reference image, without altering the reference image at all.

Most relative radiometric normalisation methods make the assumption that the function f between the subject and reference images is linear. The reference image is purely selected to represent the common radiometric scale for normalisation, and need not be the more accurate of the images in terms of true spectral levels. Relative radiometric normalisation is able to indiscriminately and simultaneously correct for several subject/reference discrepancies such as reflectance, solar angles,

atmospheric conditions and image capturing configurations, and has therefore become a widely used tool for spectral calibration between corresponding images.

2.2 Regression RRN

A regression or pseudoinverse model is the most basic form of relative radiometric normalisation. Given a subject image S and a reference image R, if all pixels in the images are used as the control set for the radiometric calibration, the linear regression model aims to find a set of parameters $\mathbf{\Theta}$ minimising the regression error $||\mathbf{R} - \mathbf{S\Theta}||_2^2$, where $\mathbf{R}$ and $\mathbf{S}$ are the feature matrices representing the spectral signatures of the reference and subject pixels respectively. The model utilises all of the pixels of the reference and subject images to estimate model parameters $\hat{\mathbf{\Theta}}$ using the pseudoinverse, i.e.,

$$\hat{\mathbf{\Theta}} = \left(\mathbf{S}^\top \mathbf{S}\right)^{-1} \mathbf{S}^\top \mathbf{R}. \tag{2.1}$$

In the case where all pixels are utilised in the radiometric alignment, regression parameters can be found through a simple pseudo-inverse. However, spectral discrepancies brought about sensor errors, clouds, shadows, atmospheric conditions and random interference noise can create individually anomalous pixels which warp yielded results and cannot be accounted for, and an additional change detection algorithm is required to detect and exclude such pixels from the analysis.

2.3 Covariance Equalisation

One such method used to exclude changed pixels from RRN is **Covariance Equalisation (CE)** [15], where inter-band covariances in the subject and reference images are matched to better detect anomalies for exclusion. Subject and reference pixel readings are transformed by finding the mean and covariance matrices for each spectral band, performing an eigendecomposition on the covariance matrices and using these components to normalise the subject and reference images to best detect anomalies. Transformations for $\mathbf{R}$ and $\mathbf{S}$ are calculated as

$$P(\mathbf{R}) = V_\mathbf{R} D_\mathbf{R}^{-1/2} V_\mathbf{R}^T \left(\mathbf{R} - \boldsymbol{\mu}_\mathbf{R}\right), \tag{2.2}$$

$$P(\mathbf{S}) = V_\mathbf{S} D_\mathbf{S}^{-1/2} V_\mathbf{S}^T \left(\mathbf{S} - \boldsymbol{\mu}_\mathbf{S}\right), \tag{2.3}$$

where $\boldsymbol{\mu}_{\mathbf{R}}$, $\boldsymbol{\mu}_{\mathbf{S}}$, $\boldsymbol{\Sigma}_{\mathbf{R}}$ and $\boldsymbol{\Sigma}_{\mathbf{S}}$ denote the band means and covariance matrices of $\mathbf{R}$ and $\mathbf{S}$ respectively, and the eigendecompositions of the covariance matrices are given by $\boldsymbol{\Sigma}_{\mathbf{R}} = V_{\mathbf{R}} D_{\mathbf{R}} V_{\mathbf{R}}^T$ and $\boldsymbol{\Sigma}_{\mathbf{S}} = V_{\mathbf{S}} D_{\mathbf{S}} V_{\mathbf{S}}^T$. Changed pixels are identified as having large residual distances $||P(\mathbf{R}) - P(\mathbf{S})||_2$. Pixels are excluded from further analysis whenever residual distances are large.

2.4 Multivariate Alteration Detection

The Multivariate Alteration Detection (MAD) algorithm [11] similarly excludes anomalous pixels from the radiometric normalisation between subject and reference images. Canonical correlation analysis is performed in order that the largest amount of variation within each band in the difference images can be accounted for [25]. This process yields MAD components, a set of orthogonal images with the same number of bands as $\mathbf{S}$ and $\mathbf{R}$, which are analysed in terms of their implied correspondence between subject and reference pixels. These components are defined by the transformation

$$\mathbf{S},\, \mathbf{R} \rightarrow \begin{bmatrix} a_{N_R}^T \mathbf{S} - b_{N_R}^T \mathbf{R} \\ \vdots \\ a_1^T \mathbf{S} - b_1^T \mathbf{R} \end{bmatrix}, \tag{2.4}$$

where $\left\{a_j,\, b_j : j \in 1, \ldots, N_R\right\}$ are the canonical coefficients from a standard correlation analysis, and N_R is the number of bands in $\mathbf{R}$. The transformation ranks its components from the highest order variates difference to the lowest.

If $\left\{\rho_j : j \in 1, \ldots, N_R\right\}$ represent the ascendingly sorted canonical correlations, the MAD components' variances are given by

$$\sigma^2_{\mathrm{MAD}_j} = 2\left(1 - \rho_{(N_R - j + 1)}\right). \tag{2.5}$$

In line with the central limit theorem, if the MAD components are standardised to unit variances, the sum of squared MAD variates should approach a χ^2 distribution with degrees of freedom given by the number of spectral bands in the subject image. The distribution of any pixel i is given by

$$T_i = \sum_{j=1}^{N_R} \frac{\mathrm{MAD}_{i,j}^2}{\sigma^2_{\mathrm{MAD}_j}} \in \chi^2_{N_R}. \tag{2.6}$$

Pixels are judged as being changed pixels based on the T_i value being above a chosen threshold p. The results of the MAD algorithm are very sensitive to the choice of this threshold, since inliership is entirely based upon this cut-off.

2.5 Iteratively Reweighted Multivariate Alteration Detection

This issue was addressed by the development of the **Iteratively Reweighted MAD (IR-MAD)** algorithm [10], which more discriminatively separates the changed from the unchanged pixels by iteratively reweighting pixels to assign higher weights to observations that do not show large changes over time.

More specifically, pixels are weighted at each iteration by weights v, which is given by the probability of a χ^2 value smaller than T_i. Iterations are performed until changes in the canonical correlation coefficients become sufficiently small between iterations. As in the MAD case, pixels are ultimately judged as being changed pixels based on the T_i value being above a pre-determined threshold p.

2.6 Iterative Slow Feature Analysis

Iterative Slow Feature Analysis (ISFA) [24] was developed as a similarly iterative method to more clearly separate changed and unchanged pixels, alternating between the calculation of variates and reweighting for better division between included and excluded pixels. Invariant features are extracted by transforming pixels into Slow Feature Analysis (SFA) variates, analysing the size of these variates, and progressively assigning larger weights to variates of smaller size, which represent unchanged pixels.

At each iteration, given a set of weights v, the set of subject and reference pixels $\mathbf{S}$ and $\mathbf{R}$ of equal band dimension N_R are normalised as

$$\hat{\mathbf{S}} = \frac{\mathbf{S} - \boldsymbol{\mu}_{\mathbf{S}}^{(v)}}{\boldsymbol{\sigma}_{\mathbf{S}}^{(v)}}, \quad \hat{\mathbf{R}} = \frac{\mathbf{R} - \boldsymbol{\mu}_{\mathbf{R}}^{(v)}}{\boldsymbol{\sigma}_{\mathbf{R}}^{(v)}} \tag{2.7}$$

where $\boldsymbol{\mu}_{\mathbf{S}}^{(v)}$, $\boldsymbol{\sigma}_{\mathbf{S}}^{(v)}$ and $\boldsymbol{\mu}_{\mathbf{R}}^{(v)}$, $\boldsymbol{\sigma}_{\mathbf{R}}^{(v)}$ are the weighted spectral band means and standard deviations of $\mathbf{S}$ and $\mathbf{R}$. Two matrices,

$$\hat{\mathbf{A}} = \boldsymbol{\Sigma}_{\Delta}^{v} \quad \text{and} \quad \hat{\mathbf{B}} = \frac{\boldsymbol{\Sigma}_{\hat{S}}^{v} + \boldsymbol{\Sigma}_{\hat{R}}^{v}}{2} \tag{2.8}$$

are computed, where $\boldsymbol{\Sigma}_{\hat{S}}^{v}$ and $\boldsymbol{\Sigma}_{\hat{R}}^{v}$ are the weighted covariance matrices for $\hat{\mathbf{S}}$ and $\hat{\mathbf{R}}$, and $\boldsymbol{\Sigma}_{\Delta}^{v}$ is the covariance matrix of the difference image $\Delta = \hat{\mathbf{S}} - \hat{\mathbf{R}}$. The generalised eigenproblem

$$\hat{\mathbf{A}}\mathbf{W} = \hat{\mathbf{B}}\mathbf{W}\boldsymbol{\Lambda}, \tag{2.9}$$

is solved, and each eigenvector w_j in $\mathbf{W}$ is normalised as

$$\hat{\boldsymbol{w}}_j = \frac{\boldsymbol{w}_j}{\sqrt{\boldsymbol{w}_j^{\mathrm{T}}\mathbf{B}\boldsymbol{w}_j}}, \tag{2.10}$$

and the SFA components $SFA_j = \hat{\boldsymbol{w}}_j^{\mathrm{T}}\hat{\mathbf{S}} - \hat{\boldsymbol{w}}_j^{\mathrm{T}}\hat{\mathbf{R}}$ are computed. The variance of these components are given by λ_j, the diagonal values of $\boldsymbol{\Lambda}$. By the central limit theorem, the sum of squared normalised SFA components approaches a χ^2 distribution with N_R degrees of freedom, i.e.,

$$T_i = \sum_{j=1}^{N_R} \frac{\left(SFA_j^i\right)^2}{\lambda_j} \in \chi^2_{N_R}. \tag{2.11}$$

Weights are recomputed as $v = P(\chi^2_{N_R} > T_k)$, and the process is repeated until changes in λ_j become sufficiently small between iterations. Changed pixels are chosen as those with weights v above a prespecified threshold p.

2.7 RANSAC and related methods

The basis for the random sampling method proposed in this research is the random sample consensus (RANSAC) algorithm put forward by Fischler and Bolles [5]. The original use of RANSAC is for geometric calibration between images, where small sets of random pixels are sampled from two images in order to geometrically align them through transformations such as the fundamental matrix, essential matrix or

a homography. This research seeks to justify the use of a RANSAC-based methodology for radiometric calibration justified by its similarity to the core methodology of geometric calibration, where a regression-based model with a specified performance metric is also utilised to detect and exclude outliers.

In line with the random sampling relative radiometric normalisation method proposed in this research, strategies for the preweighting of pixels in the random sampling are also proposed. The Simple Linear Iterative Clustering (SLIC) algorithm developed by Achanta et al. [1] utilises a k-means clustering related method to segment images into clusters of pixels with similar radiometric characteristics and spatial positioning, which are referred to as superpixels. The creation of superpixels is justified for the use in this research, since the clustering of similar pixels allows for a more refined sampling strategy to more definitively discriminate between inlier and outlier pixel groups.

Based on the conducted research and thorough literature consultation, no paper was found which specifically used a random sampling-based approach for RRN. The most commonly used existing methods with a similar objective (namely Covariance Equalisation, Multivariate Alteration Detection, Iteratively Reweighted Multivariate Alteration Detection and the Iterative Slow Feature Analysis) have been used within the literature survey and as part of the analysis to provide a comparison to the method proposed in this research.

2.8 Structural Similarity Index Measure

The structural similarity index measure (SSIM) developed by Wang et al. [21] provides a metric whereby the quality of spectral calibration between two geometrically calibrated images can be analysed. More specifically, discrepancies between corresponding images are considered as the perceived changes in the structural information between one image and the other.

For any two images x and y, the SSIM score is calculated as

$$\mathrm{SSIM}(x,y) = \frac{\left(2\mu_x\mu_y + c_1\right)\left(2\sigma_{xy} + c_2\right)}{\left(\mu_x^2 + \mu_y^2 + c_1\right)\left(\sigma_x^2 + \sigma_y^2 + c_2\right)}, \tag{2.12}$$

where $c_1 = (k_1 L)^2, c_2 = (k_2 L)^2$ are variables added to prevent instability when denominators are close to 0, and L is given by the dynamic range of possible pixel spectral readings. k_1 and k_2 are respectively set to 0.01 and 0.03 by default. The SSIM score is based on three functions between images x and y, namely the luminance comparison $\mathbf{l}$, the contrast comparison $\mathbf{c}$ and the structure comparison $\mathbf{s}$. These comparison functions are computed as

$$\mathbf{l}(x,y) = \frac{2\mu_x\mu_y + c_1}{\mu_x^2 + \mu_y^2 + c_1} \tag{2.13}$$

$$\mathbf{c}(x,y) = \frac{2\sigma_x\sigma_y + c_2}{\sigma_x^2 + \sigma_y^2 + c_2} \tag{2.14}$$

$$\mathbf{s}(x,y) = \frac{2\sigma_{xy} + c_2}{2\sigma_x\sigma_y + c_2}, \tag{2.15}$$

where (μ_x, σ_x) and (μ_y, σ_y) are the means and standard deviations of the two images' spectral readings, and σ_{xy} is their covariance. The overall SSIM score is given by the product of these functions

$$\text{SSIM}(x,y) = \mathbf{l}(x,y).\mathbf{c}(x,y).\mathbf{s}(x,y) \tag{2.16}$$

Chapter 3

Research Methodology

3.1 Research design

A confirmatory experimental approach is utilised in the research methodology. In order to calibrate any pair of images, spectral adjustments are performed on the subject image, to more closely align to the reference image. The structural similarity index (SSIM) as developed by Wang et al. [21] provides a measure of the similarity between the corresponding images. In the analysis of the proposed algorithm outputs, the SSIM measure will be used along with the mean squared error (MSE) and the peak signal-to-noise ratio to gauge the similarity between the outputted images under each of the radiometric calibration schemes. Ideal calibrations would be optimised to the lowest MSE and highest PSNR, and the yielded SSIM must be as high as possible.

The research posits that the similarity scores of multispectral images aligned through RRN will be improved by utilising a random sampling methodology based on RANSAC to exclude outlier pixels from the analysis. It seeks to confirm this by applying the relative radiometric normalisation method in conjunction with a random sampling methodology, and testing the accuracy with which inlier pixels match destination pixels after normalisation.

The random sampling methodology will be applied using uniform weighting, as well as variations using pre-weighting, and results will be compared in terms of accuracies and computing times. Random sampling RRN will then be compared to the CE, MAD, IR-MAD and ISFA algorithms in terms of running times, performance and calibrated image similarity scores.

3.2 Data

Co-registered satellite image pairs, as shown in Fig. 3.1, are used as test data. These image pairs have various size and band specifications, and are obtained from the Google Earth application, the Sentinel EO Browser and the QGIS application together with satellite data importation plugins. Images are co-registered by their respective built-in satellite co-ordinate system software.
Descriptions of each of the image pairs are given as follows:

(a) 128×128 pixel, true-colour images of Lake Ngezi, Matebeleland South Province, Zimbabwe captured in August 2020 and December 1991 by Landsat 8 and 7 satellites, demonstrating the decrease in dam levels due to increased water consumption.

(b) 256×256 pixel, 12-band images of Lake Ankarakaraka, Antananarivo Province, Madagascar captured in November 2018 (Spring) and May 2020 (Autumn) by Sentinel-2 satellites, showing seasonal changes in agricultural farmland.

(c) 386×386 pixel, true-colour images of the Katse Dam area, Thaba-Tseka Province, Lesotho captured in December 1991 and December 2016 by Landsat 7 and 8 satellites, showing the construction of the reservoir.

(d) 512×512 pixel, true-colour images of Theewaterskloof Dam, Western Cape, South Africa captured in October 2020 (Spring) and March 2018 (Autumn) by Landsat 8 and Sentinel-2 satellites, showing seasonal changes and additional glare in the reference image.

(e) 640×640 pixel, 12-band images of the Drakensberg, KwaZulu-Natal, South Africa captured in June 2020 and June 2017 by Sentinel-2 satellites, showing different solar angles and small physical changes in the landscape.

(f) 300×300 pixel, 6-band images of Lago di Mulargia, Cagliari, Italy captured in September 2002 (Autumn) and May 2003 (Spring) by Landsat 7 satellites, demonstrating the seasonal change in water levels due to winter rainfall.

(g) 700×700 pixel, 8 and 7-band images of Palm Jumeirah, Dubai City, United Arab Emirates captured in May 2003 and September 1990 by Landsat 7 and 5 satellites, showing the construction of the Palm Jumeirah archipelago.

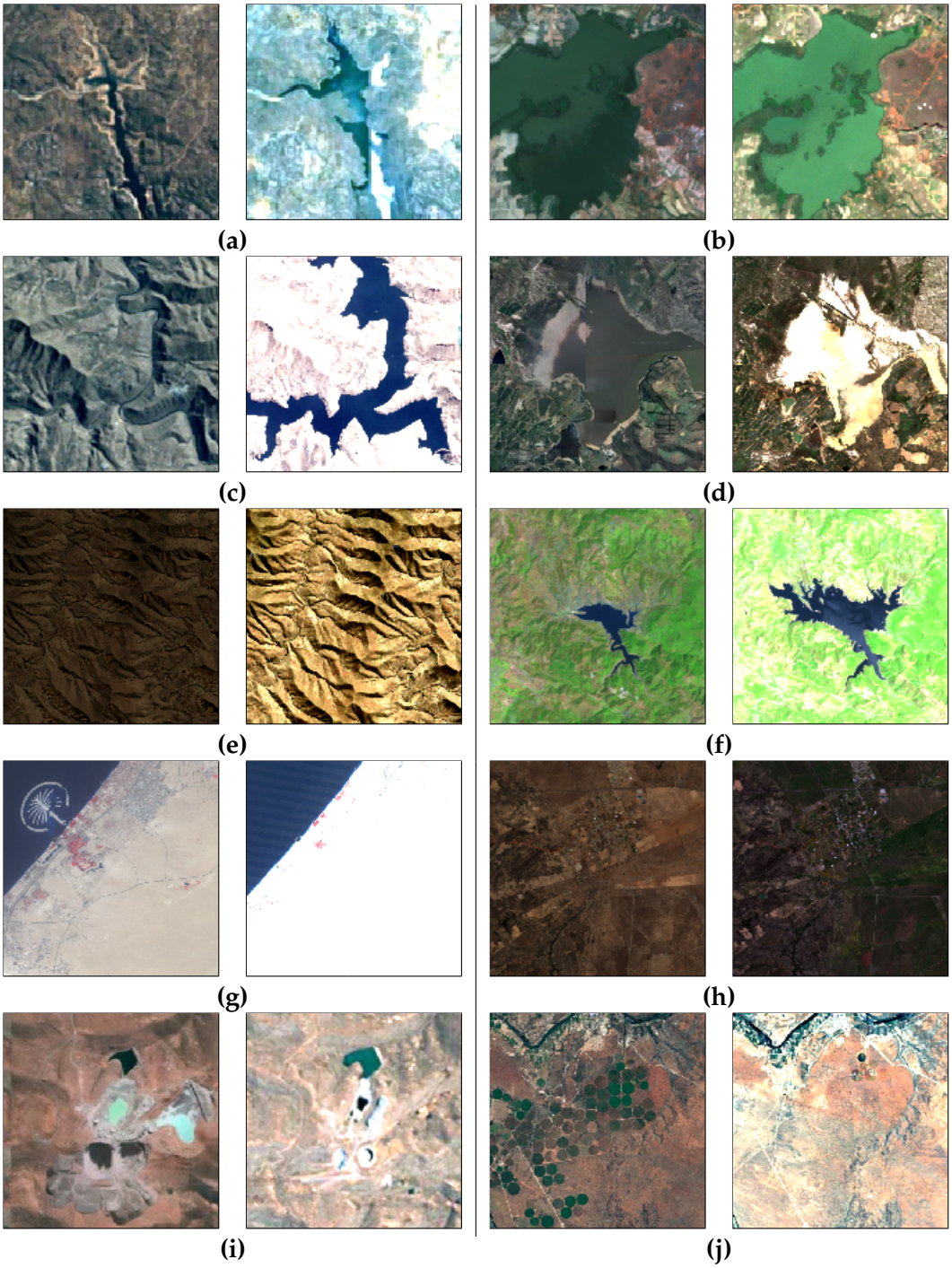


FIGURE 3.1: True-colour renderings of test subject (left) and reference (right) images of (a) Lake Ngezi, (b) Lake Ankarakaraka, (c) Katse Dam, (d) Theewaterskloof Dam, (e) Drakensberg, (f) Lago di Mulargia, (g) Palm Jumeirah, (h) Nieuwoudtville, (i) Letšeng mine, and (j) Douglas

(h) 264 × 264 pixel, 12-band images of Nieuwoudtville, Northern Cape, South Africa captured in February 2020 (Summer) and September 2020 (Spring) by Sentinel-2 satellites, showing seasonal changes in the area landscape due to winter rainfall.

(i) 256 × 256 pixel, true-colour images of Letšeng diamond mine, Lesotho captured in August 2020 and December 1990 by Landsat 8 and 7 satellites, showing the increase in the area of mining activity.

(j) 512 × 512 pixel, true-colour images of Douglas, Northern Cape, South Africa captured in June 2016 (Winter) and December 1986 (Summer) by Landsat 8 and 7 satellites, showing the increase in irrigated agricultural land around the Orange River.

It is important to note that CE, IR-MAD and ISFA can only perform band-to-band normalisation, so for image (d), RRN is performed only on the true colour (or visible) bands in both the Landsat-8 and Sentinel-2 images. Similarly, in image (g), RRN can only be applied through CE, IR-MAD and ISFA using the 7 corresponding bands of the Landsat 7 and 5 satellite imagery. Such a limitation does not apply to the Random Sampling-based algorithms proposed in the research.

3.3 Proposed method

3.3.1 Random Sampling-based RRN (RS-RRN)

The performance of relative radiometric normalisation is highly dependent on selection of a good and representative inlier subset. This research puts forward a random sampling approach, specifically random sample consensus (RANSAC) [5], to effectively select inlier subsets. Although RANSAC was developed for geometric calibration applications, its core methodology can be utilised to detect and exclude outliers for any regression-based model with a specified performance metric. This paper focuses on the novel use of random sampling in the radiometric calibration of geometrically co-registered multiband images. The proposed Random Sampling-based RRN (RS-RRN) iteratively learns a multivariate regression model from randomly sampled minimal-size subsets of pixels which results in a significant reduction in computing times. The RS-RRN employs an adaptive pixel weighting

Algorithm 1 Random Sampling-based RRN (RS-RRN)

procedure RS-RRN($S, R, s, d, \eta_0, k_{max}$)
  $MSE^* \leftarrow \infty$
  for $k = 1 : k_{max}$ **do**
    Generate hypotheses through sampling:
      Sample the minimal pixel subset $\mathbf{R}^k$ and $\mathbf{S}^k$
      Estimate model parameters $\hat{\mathbf{\Theta}}^k$ using Eq. (3.1)
    Verify the generated model:
      Calculate the MSE, $MSE_{\hat{\mathbf{\Theta}}^k}$ for the $\hat{\mathbf{\Theta}}^k$ model
    if $MSE_{\hat{\mathbf{\Theta}}^k} < MSE^*$ **then**
      $\mathbf{\Theta}^* \leftarrow \hat{\mathbf{\Theta}}^k, \quad MSE^* \leftarrow MSE_{\hat{\mathbf{\Theta}}^k}$
      Find $\mathcal{I}^*$, the set of pixels with residuals $< d$
      Calculate $\epsilon = |\mathcal{I}^*|/N$, the proportion of inliers
      Recalculate $k_{max} \geq \frac{log(1-\eta_0)}{log(1-\epsilon)} \times m$
    end if
  end for
  Generate non-minimal sample models with $\mathcal{I}^*$ and $\mathbf{\Theta}^*$
end procedure

method to increase the likelihood of pixels with smaller spectral differences in reference and subject in random sampling process, which yields improved convergence time and robustness against the outlier (or changed) pixels. Unlike the CE, IR-MAD and ISFA algorithms, RS-RRN can also operate on reference and subject images with different numbers of spectral bands.

As shown in **Algorithm 1**, RS-RRN consists of randomly selecting several corresponding pixel subsets from subject and reference images, creating regression models for each of these subsets, and using the model of lowest mean squared error to determine the set of unchanged pixels as those below a prespecified threshold distance from the regression predictions.

Given a subject image S and a reference image R, k_{max} regression models are sequentially created using pixel subsets from S and R of size s. For each regression model $\hat{\mathbf{\Theta}}^k$, pixels in the subset are linearly mapped as $\mathbf{R}_i = \mathbf{S}_i\hat{\mathbf{\Theta}}^k$, where $\mathbf{R}_i \in 1 \times \mathbb{R}^{N_R}$ and $\mathbf{S}_i \in 1 \times \mathbb{R}^{N_S}$ represent the spectral signatures of pixel $i \in \{1, \ldots, s\}$ in the subject and reference pixel subsets $\mathbf{R}^k \in \mathbb{R}^{s \times N_R}$ and $\mathbf{S}^k \in \mathbb{R}^{s \times N_S}$. $\hat{\mathbf{\Theta}}^k \in \mathbb{R}^{N_S \times N_R}$ is a matrix of parameters that linearly maps the subject image pixels to the reference image where N_R represents the number of spectral bands in R, while N_S represents

the total number of bands in S plus one, which allows for intercept parameters. The parameter matrix $\hat{\mathbf{\Theta}}^k$ is computed according to

$$\hat{\mathbf{\Theta}}^k = \left({\mathbf{S}^k}^\top \mathbf{S}^k + \lambda \mathbf{I} \right)^{-1} {\mathbf{S}^k}^\top \mathbf{R}^k \tag{3.1}$$

where $\lambda = 0.1$ is an arbitrarily small regularization constant and $\mathbf{I} \in \mathbb{R}^{N_S \times N_S}$ is the identity matrix. Although the RS-RNN can operate with different minimal set sizes satisfying $s \geq 2$, the value $s = 2$ is deliberately chosen to reduce computing times and keep the likelihood of selecting the changed (or outlier) pixels low. Thus, the regularised pseudoinverse Eq. (3.1) is used instead of Eq. (2.1) in estimating the model parameters to regularise the matrix inversion.

The model $\mathbf{\Theta}^*$ of lowest mean squared error is considered, and the set $\mathcal{I}^*$ containing all pixels i from the full set having regression errors $||\mathbf{R}_i - \mathbf{S}_i \mathbf{\Theta}^*||_2$ smaller than d is chosen as the unchanged set of pixels used in the final model.

To decrease computing times, k_{max} is adaptively rationalised based on the proportion of pixels which are inliers, $\epsilon = \frac{|\mathcal{I}^*|}{N}$, and a prespecified threshold parameter η_0, representing the desired confidence level that at least one of the samples k is uncontaminated. RS-RRN requires the calibration of two parameters, d and η_0, as inputs. A large d value results in the model including more potentially outlying pixels, while a smaller value may exclude important high-leverage inlier readings vital to the analysis. The η_0 reading is used in the adaptive rationalisation of k_{max}, and higher η_0 enforces more stringent measures to obtain an uncontaminated sample, but increase computing times. To carefully calibrate these parameters, a regression model is performed between the entire subject and reference images, and the model's residuals are considered. d is chosen as

$$d^* = \underset{d}{\operatorname{argmin}} \left\{ d / q_d^2 \right\}, \tag{3.2}$$

where q_d is the distribution percentile of distance d, and η_0 is chosen as the corresponding q_{d^*}.

s is chosen as 2, since the algorithm seeks uncontaminated samples, and the probability of contamination with outlier pixels increases exponentially as s is increased. $s = 2$ is the smallest subset in $\mathbf{R}$ which cannot be adequately specified using only intercept parameters. As proposed in [5], k_{max} is multiplied by $m = 3$ to

ensure a larger sampling pool.

3.3.2 Weighted RS-RRN

An extension to the standard RS-RRN algorithm proposed above is the Weighted RS-RRN. In order that pixels with smaller errors are more likely to be sampled, and fewer hypotheses would be required to find the best model, each pixel is weighted according to their likelihoods of giving models with better subject-reference image correspondences. A linear regression model is made between the full subject and reference images, and each pixel i is weighted according to the inverse of the regression standard errors, i.e.,

$$w_i = 1/||\mathbf{R}_i - \mathbf{S}_i\mathbf{\Theta}^*||_2. \tag{3.3}$$

The RS-RRN algorithm is then performed as in **Algorithm 1**, using these weights during each sampling step.

3.3.3 SLIC RS-RRN

Simple Linear Iterative Clustering (SLIC) is used to cluster spatially and spectrally related pixels into superpixels which can also then be used as a basis for more refined sampling weights in the RS-RRN algorithm.

A value L is chosen as the approximate number of similarly sized superpixel clusters into which the entire set of pixels must be divided. The subject image S and a reference image R are superimposed into one single image with $N_S + N_R$ spectral bands.

$l \in \{1, 2, \ldots, L\}$ equally spaced centroid positions are chosen from the full image extent with grid step sizes given by G, the distance between centroid positions. Cluster centres C_l are chosen as $[\mathbf{S}_l, \mathbf{R}_l, x_l, y_l]^T$, where $\mathbf{S}_l$ denotes the spectral signature of pixel l of S, $\mathbf{R}_l$ denotes the spectral signature of pixel l of R, and x_l and y_l denote the horizontal and vertical positioning of l within the image.

For each cluster centre C_l and pixels i within a $2G \times 2G$ vicinity around C_l, distances between i and C_l are computed, and, if C_l is the cluster centre to which pixel i is the closest in terms of its spectral signatures, i is assigned to cluster l. Cluster centres C_l are then recomputed using the average spectral and spatial values of all

pixels contained in l. This procedure is repeated until a suitably low error threshold is reached.

Weights can then be assigned to pixels within the RS-RRN routine based on their superpixel characteristics. Given a superpixel l, a linear regression model is made between all pixels i of the subject and reference images contained in l, and pixels $i \in l$ are weighted according to the inverse of the regression root mean squared error, i.e.,

$$w_i = \frac{1}{\sqrt{\sum_{i \in l} (\mathbf{R}_i - \mathbf{S}_i \mathbf{\Theta}^l)^2}} \tag{3.4}$$

where $\mathbf{\Theta}^l$ is the parameter matrix for the least squares regression model for set l.

The clusters parameter L needs to be determined as an input for any pair of images before analysis, so the SLIC RS-RRN algorithm cannot be fully automatically calibrated as in the case of the standard or weighted RS-RRN algorithms. A larger number of superpixel clusters L linearly increases computing times, but also decreases pixel group sizes, resulting in more fragmented readings with poorer scalability to the full image. Smaller L values may result in larger superpixels, which may inadvertently include anomalous pixels within superpixel clusters. Images containing a higher number of distinct features or zones generally require a higher number of superpixels to be analysed.

3.4 Analysis

Tested image pairs are radiometrically calibrated with ordinary regression using Eq. (2.1), and then r RS-RRN and the parameter optimised CE, MAD, IR-MAD and ISFA algorithms.

More specifically, the structural similarity index measure (SSIM) as developed by Wang et al. [21] is used as the measure of similarity between the tested subject and reference images. In the analysis of the proposed algorithm outputs, the SSIM measure will be used along with the mean squared error (MSE) and the peak signal-to-noise ratio (PSNR) to gauge the similarity between the outputted images under each of the radiometric calibration schemes. Computing times are also compared to gauge each algorithms' efficiency.

TABLE 3.1: Optimised parameters for the spectral calibration methodologies

	CE	**MAD**	**IR-MAD**		**ISFA**		**SLIC RS-RRN**
Image pair	q	p	p	δ	p	q_v	L
(a)	1.00	0.190	10^{-7}	0.01	0.01	0.90	30
(b)	0.91	0.960	0.1	0.10	10^{-9}	0.82	10
(c)	1.00	0.000	10^{-16}	0.01	10^{-15}	0.83	45
(d)	0.70	0.200	10^{-15}	0.01	10^{-10}	0.81	20
(e)	0.64	0.003	10^{-5}	0.10	10^{-15}	0.73	40
(f)	0.64	0.550	10^{-3}	0.10	10^{-6}	0.65	40
(g)	0.80	0.890	10^{-6}	0.01	10^{-15}	0.11	30
(h)	0.07	0.000	0	1.00	10^{-15}	0.98	20
(i)	0.88	0.010	10^{-11}	0.10	0.10	0.93	25
(j)	1.00	0.000	0	1.00	10^{-10}	0.96	20

Calibrations for the CE, MAD, IR-MAD, ISFA and SLIC RS-RRN algorithms are explicitly optimised to the highest yielded SSIM through a simultaneous grid-search procedure of all variable combinations, while each of these algorithms by their nature seek to minimise the mean squared error between the subject and reference images,

$$MSE = \frac{1}{|\mathcal{I}^*|} \sum_{i \in \mathcal{I}^*} (\mathbf{R}_i - \mathbf{S}_i \mathbf{\Theta}^*)^2, \tag{3.5}$$

which in turn maximises $PSNR = -10 \log_{10} (MSE)$. This is explored in the next section.

3.5 Parameter Optimisation

While the input parameters for the proposed random sampling RRN and the weighted random sampling RRN methods are either adaptively calculated or can be fixed, the CE, MAD, IR-MAD and ISFA algorithms require the calibration of parameters to yield the highest SSIM score. Similarly, the SLIC extension to the RS-RRN algorithm needs parameter pre-calibration for optimal results.

The CE algorithm requires the choosing of a quantile threshold q, which represents the quantile where the distribution of the residual distances $||P(\mathbf{R}) - P(\mathbf{S})||_2$ is clipped to exclude outliers, which are the pixels of highest residual distance.

The MAD algorithm requires the calibration of the probability threshold p, which represents the probability of obtaining a higher χ^2 than the normalised sum of squared variates shown in Eq. (2.6).

Similarly, the threshold p is also required for the IR-MAD algorithm, together with a convergence threshold parameter δ which represents the maximum permitted changes in canonical correlation coefficients between iterations for convergence. Convergence is assumed to have occurred when changes in every correlation coefficient between iterations is smaller than δ.

The ISFA algorithm requires the calibration of two parameters, p and q_w. p represents the probability of a χ^2 value larger than the normalised sum of squared SFA variates shown in Eq. (2.11), and q_v is a threshold input used in determining the initial weights v. More specifically, a full regression model is performed, the distribution of the residuals is considered, and all pixels showing residuals below the q_v quantile are weighted as 1 and those above are weighted as 0.

The SLIC RS-RRN requires the calibration of the superpixel number L which determines the approximate number of superpixel clusters l into which the pixels will be divided.

Parameters are optimised using a grid-search routine. Each of the ten pairs of images have different optimal parameter values under each RRN scheme. These are shown in Table 3.1.

It is important to note that for image pairs (a), (c) and (j), the CE algorithm is optimised when the quantile threshold score is set to 1, meaning all pixels are included in the analysis. This is equivalent to using regression RRN, since no anomalous pixels are excluded from the analysis.

Similarly, for image pairs (c), (h) and (j), the optimal probability threshold p for the MAD algorithm is 0, meaning that all MAD variates fall above the threshold, and all pixels are included in the analysis. This means that MAD is unable to find a better control set than the baseline linear model. Iterative reweighting also does not prove to find a control set better than that of the standard MAD algorithm for image pairs (h) and (j), so the regression threshold p is also equal to 0 in the IR-MAD case for these image pairs.

Chapter 4

Results and Discussion

4.1 Quantitative comparisons

4.1.1 Comparison of RS-RRN algorithms

The weighted random sampling RRN generally performs similarly to the uniform random sampling RRN algorithm in terms of the structural similarity index measure, with all structural similarity and peak signal-to-noise ratio scores in the same range, and shows only a slight increase in computational times for image pairs with higher numbers of bands (i.e.: image pairs (b), (e), (f) and (g)), although the difference is not statistically significant. It also consistently performs in the same range of SSIM scores as the SLIC RS-RRN algorithm, while demonstrating superior computation times. The SLIC RS-RRN is the most sensitive in terms of computation times to the number of spectral bands. All of the RS-RRN algorithms converge as the number of samples k_{max} is increased, but the weighted RS-RRN shows a smaller range of SSIM, MSE and PSNR values within its different iterations when the designated k_{max} recalculation scheme is applied, demonstrating better convergence within the larger random sampling algorithm scheme. Computational times also do not include times for paramater calibrations for L in the SLIC algorithm, which further decrease its efficiency.

Overall, the weighted RS-RRN algorithm is found to perform the best amongst the random sampling-based RRN methods, since it consistently achieves high and consistent SSIM and PSNR scores without large computing times. For this reason, it is the weighted RS-RRN that is further considered for comparison against other widely used relative radiometric normalisation methods.

TABLE 4.1: SSIM comparisons of 100 trials of RS-RRN methods

Image pair	Metric	RS-RRN	Weighted RS-RRN	SLIC RS-RRN	Image pair	Metric	RS-RRN	Weighted RS-RRN	SLIC RS-RRN
(a)	Mean:	0.626	0.637	0.632	**(f)**	Mean:	0.839	0.837	0.840
	SD:	0.017	0.006	0.008		SD:	0.004	0.003	0.003
(b)	Mean:	0.834	0.836	0.837	**(g)**	Mean:	0.877	0.875	0.878
	SD:	0.006	0.005	0.005		SD:	0.003	0.004	0.001
(c)	Mean:	0.655	0.658	0.656	**(h)**	Mean:	0.882	0.885	0.882
	SD:	0.007	0.003	0.006		SD:	0.003	0.001	0.004
(d)	Mean:	0.615	0.632	0.623	**(i)**	Mean:	0.819	0.820	0.820
	SD:	0.030	0.006	0.020		SD:	0.005	0.001	0.003
(e)	Mean:	0.798	0.799	0.798	**(j)**	Mean:	0.761	0.768	0.763
	SD:	0.007	0.008	0.006		SD:	0.009	0.001	0.006

TABLE 4.2: MSE comparisons of 100 trials of RS-RRN methods

Image pair	Metric	RS-RRN	Weighted RS-RRN	SLIC RS-RRN	Image pair	Metric	RS-RRN	Weighted RS-RRN	SLIC RS-RRN
(a)	Mean:	0.0059	0.0061	0.0060	**(f)**	Mean:	0.0054	0.0056	0.0053
	SD:	0.0004	0.0001	0.0004		SD:	0.0004	0.0003	0.0004
(b)	Mean:	0.0176	0.0184	0.0171	**(g)**	Mean:	0.0028	0.0027	0.0028
	SD:	0.0020	0.0018	0.0023		SD:	0.0002	0.0004	0.0001
(c)	Mean:	0.0124	0.0118	0.0117	**(h)**	Mean:	0.0121	0.0125	0.0111
	SD:	0.0034	0.0021	0.0029		SD:	0.0014	0.0009	0.0014
(d)	Mean:	0.0278	0.0350	0.0242	**(i)**	Mean:	0.0038	0.0039	0.0038
	SD:	0.0087	0.0072	0.0087		SD:	0.0001	0.00004	0.0001
(e)	Mean:	0.0290	0.0288	0.0292	**(j)**	Mean:	0.0067	0.0070	0.0067
	SD:	0.0018	0.0015	0.0017		SD:	0.0002	0.0001	0.0002

TABLE 4.3: PSNR comparisons of 100 trials of RS-RRN methods

Image pair	Metric	RS-RRN	Weighted RS-RRN	SLIC RS-RRN	Image pair	Metric	RS-RRN	Weighted RS-RRN	SLIC RS-RRN
(a)	Mean:	22.30	22.10	22.20	**(f)**	Mean:	25.50	25.70	25.50
	SD:	0.30	0.10	0.30		SD:	0.30	0.20	0.30
(b)	Mean:	17.60	17.40	17.70	**(g)**	Mean:	22.20	22.50	22.70
	SD:	0.50	0.40	0.60		SD:	0.40	0.60	0.20
(c)	Mean:	19.20	19.30	19.40	**(h)**	Mean:	19.20	19.00	19.60
	SD:	1.10	0.70	0.90		SD:	0.50	0.30	0.50
(d)	Mean:	15.80	14.60	16.40	**(i)**	Mean:	24.20	24.10	24.20
	SD:	1.30	0.90	1.30		SD:	0.10	0.04	0.10
(e)	Mean:	15.40	15.40	15.40	**(j)**	Mean:	21.70	21.60	**21.70**
	SD:	0.30	0.20	0.30		SD:	0.20	0.04	0.20

TABLE 4.4: Time comparisons of 100 trials of RS-RRN methods

Image pair	Metric	RS-RRN	Weighted RS-RRN	SLIC RS-RRN	Image pair	Metric	RS-RRN	Weighted RS-RRN	SLIC RS-RRN
(a)	Mean:	0.019*s*	0.022*s*	0.09*s*	**(f)**	Mean:	0.25*s*	0.28*s*	0.78*s*
	SD:	0.004s	0.003s	0.001s		SD:	0.03s	0.02s	0.04s
(b)	Mean:	0.39*s*	0.40*s*	1.00*s*	**(g)**	Mean:	3.06*s*	3.72*s*	5.58*s*
	SD:	0.05s	0.07s	0.07s		SD:	0.56s	1.21s	0.49s
(c)	Mean:	0.29*s*	0.31*s*	0.92*s*	**(h)**	Mean:	0.44*s*	0.45*s*	1.10*s*
	SD:	0.02s	0.03s	0.04s		SD:	0.07s	0.05s	0.003
(d)	Mean:	0.65*s*	0.69*s*	1.05*s*	**(i)**	Mean:	0.10*s*	0.10*s*	0.37*s*
	SD:	0.08s	0.09s	0.05s		SD:	0.01s	0.01s	0.01s
(e)	Mean:	3.00*s*	3.26*s*	7.10*s*	**(j)**	Mean:	0.67*s*	0.75*s*	1.90*s*
	SD:	0.23s	0.43s	0.32s		SD:	0.05s	0.09s	0.37s

As shown in Table 4.5, the weighted RS-RRN demonstrates the highest average SSIM score in six of the ten data cases in the experimental trials, while ISFA yields a marginally higher SSIM than that of the weighted RS-RRN for image pairs (c), (i) and (j), and IR-MAD yields the highest SSIM for image pair (f). As demonstrated in Tables 4.1 to 4.4, it cannot be concluded that the weighted RS-RRN performs more poorly than these methods, and that lower scores may be due to statistical variation inherent in the sampling mechanism. In addition to this, the weighted RS-RRN algorithm is shown to yield a SSIM score with a significant improvement over the CE method in five out of ten of the image pair cases and a significant improvement over the MAD method for six of the ten image pairs.

In terms of the PSNR, the weighted RS-RRN is able to perform better on average than all the other algorithms in five out of the ten cases, while performing in the same range of results for the other five cases. PSNR scores of the weighted RS-RRN are significantly higher than the MAD algorithm scores in nine out of ten cases, significantly higher than the CE algorithm scores in eight of those cases, and significantly higher than the IR-MAD and ISFA algorithm scores in six and five out of ten cases respectively. In three image pair cases, namely (h), (i) and (j), the weighted RS-RRN is demonstrated to yield PSNR scores statistically lower than those of the ISFA algorithm, and statistically lower than the CE algorithm for data pair (h). The MAD and IR-MAD algorithms yield significantly higher PSNR scores than the weighted RS-RRN algorithm for image pair (b). This is reflective of the RS-RRN algorithm explicitly maximising the SSIM scores, which may be associated with a minor sacrifice in associated PSNR scores. The other algorithms maximise

TABLE 4.5: Comparison against other RRN methods

Image	Metric	Regression	Weighted RS-RRN	CE	MAD	IR-MAD	ISFA
(a)	SSIM:	0.588	**0.637**	0.588	0.597	0.630	0.634
	MSE:	0.050	**0.006**	0.050	0.025	0.010	0.007
	PSNR:	13.00	**22.10**	13.00	13.00	20.20	21.40
	Time:		**0.02s**	0.08*s*	0.07*s*	0.40*s*	0.11*s*
(b)	SSIM:	0.821	**0.836**	0.825	0.827	0.824	0.835
	MSE:	0.053	0.018	0.045	**0.006**	0.012	0.024
	PSNR:	12.70	17.40	13.50	**22.20**	19.00	16.20
	Time:		**0.40s**	**0.40s**	**0.40s**	1.00*s*	4.30*s*
(c)	SSIM:	0.602	0.658	0.602	0.602	**0.659**	**0.659**
	MSE:	0.104	0.012	0.104	0.104	**0.009**	0.012
	PSNR:	9.80	19.30	9.80	9.80	**20.60**	19.40
	Time:		**0.30s**	0.50*s*	0.60*s*	4.60*s*	1.00*s*
(d)	SSIM:	0.572	**0.632**	**0.632**	0.576	0.628	0.573
	MSE:	0.132	0.034	0.032	0.086	**0.022**	0.118
	PSNR:	8.80	14.60	14.90	10.60	**16.60**	9.30
	Time:		**0.70s**	0.90*s*	1.00*s*	6.20*s*	1.50*s*
(e)	SSIM:	0.784	**0.799**	0.791	0.785	0.786	0.784
	MSE:	0.060	**0.030**	0.048	0.053	0.051	0.049
	PSNR:	12.20	**15.40**	13.20	12.70	12.90	13.10
	Time:		3.30*s*	**2.60s**	3.00*s*	6.60*s*	33.50*s*
(f)	SSIM:	0.805	0.837	0.837	0.841	**0.843**	0.842
	MSE:	0.037	**0.006**	0.014	0.007	0.008	0.009
	PSNR:	14.30	**22.50**	18.60	21.80	20.90	20.40
	Time:		**0.30s**	0.90*s*	0.50*s*	2.70*s*	3.90*s*
(g)	SSIM:	0.856	**0.875**	0.874	0.867	0.871	**0.875**
	MSE:	0.029	**0.003**	0.022	0.004	0.006	0.015
	PSNR:	15.40	**25.70**	16.50	24.40	15.10	18.40
	Time:		3.70*s*	**2.30s**	2.70*s*	11.60*s*	35.20*s*
(h)	SSIM:	0.856	**0.885**	0.873	0.866	0.866	0.868
	MSE:	0.032	0.012	0.006	0.031	0.031	**0.001**
	PSNR:	14.90	19.10	22.50	15.10	15.10	**32.30**
	Time:		**0.40s**	1.00*s*	0.50*s*	1.10*s*	5.80*s*
(i)	SSIM:	0.815	0.820	0.816	0.816	0.816	**0.822**
	MSE:	0.017	0.004	0.012	0.011	0.013	**0.002**
	PSNR:	17.60	24.10	19.40	19.50	19.00	**27.20**
	Time:		**0.10s**	1.00*s*	0.30*s*	0.80*s*	0.40*s*
(j)	SSIM:	0.767	0.768	0.767	0.767	0.767	**0.769**
	MSE:	0.026	0.007	0.026	0.026	0.026	**0.005**
	PSNR:	15.90	21.60	15.90	15.90	15.90	**22.70**
	Time:		**0.80s**	1.00*s*	1.00*s*	2.00*s*	1.80*s*

PSNR by their nature, since their algorithms are constructed to decrease overall residual distances.

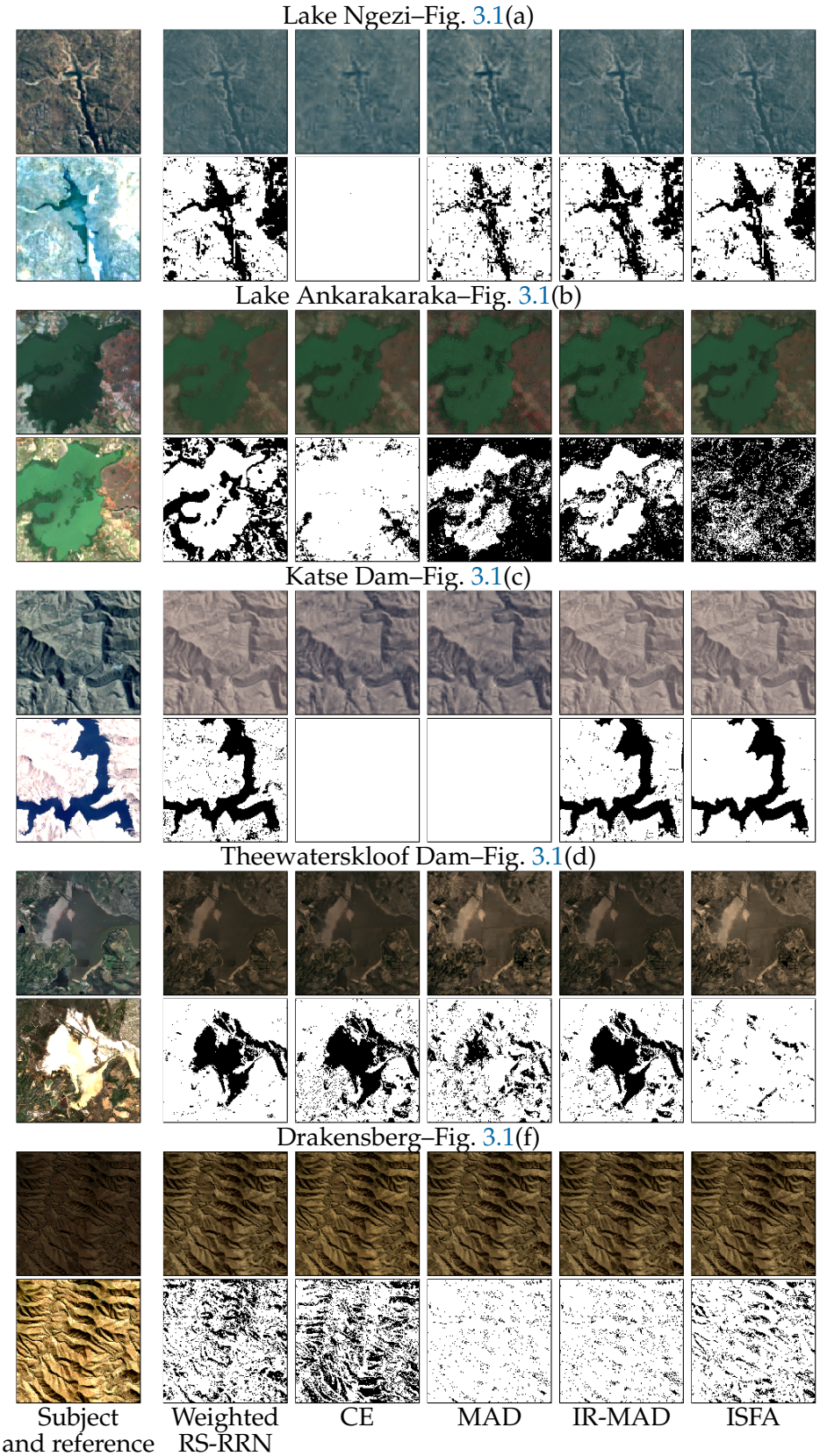
The weighted RS-RRN also consistently achieves lower computing times than IR-MAD or ISFA, and lower than CE and MAD in all but one out of ten cases. Weighted RS-RRN computing times are also less sensitive to the total number of pixels in the images, and computational improvement over the IR-MAD and ISFA models is most apparent for larger-sized image pairs, i.e., (d), (e) and (g). ISFA's computing times are the most sensitive to the number of spectral bands, as can be seen in the disproportionate running times for image pairs (b), (e), (g) and (h). The weighted RS-RRN also does not require computation time for paramter calibration as the other algorithms do, which further asserts its computational superiority.

4.2 Qualitative comparisons

The normalised subject images and corresponding change maps for each of the test image pairs resulting from different RRN methods are shown in Fig. 4.1. In change maps, the pixels displayed in black are outlier pixels detected by RRN methods, and are excluded from the RRN process. Change maps in particular are used to support visual comparisons between reference and normalised subject images.

The normalised subject images in Fig. 4.1 show that the weighted RS-RRN, IR-MAD and ISFA produce visually similar results which are better than those produced by CE and MAD. The change maps under the weighted RS-RRN are also found to show the key image features, like those of the IR-MAD and ISFA for each of the image pairs, with visibly changed features identified as outliers by all three of these methods. This is mainly due to the sampling strategy employed by the weighted RS-RRN and the iterative reweighting by ISFA and IR-MAD.

In three out of ten cases ((a), (c) and (i)), areas representing visible discrepancies between image pairs are not identified as outliers by CE, and in cases (c) and (i), visible changes are not identified as such by MAD. More specifically, MAD and CE are unable to find a control set that yields a better SSIM than that of the full regression model, so the change maps show the entire images as inlier pixels. This can be further seen by the corresponding SSIM, MSE and PSNR scores in Table 4.5, which are equal to those of the regression SSIM. Pixels in these image pairs have a very smooth correlation distribution without a clear grouping of inlier pixels to


Lake Ngezi–Fig. 3.1(a)
Lake Ankarakaraka–Fig. 3.1(b)
Katse Dam–Fig. 3.1(c)
Theewaterskloof Dam–Fig. 3.1(d)
Drakensberg–Fig. 3.1(f)
Subject and reference
Weighted RS-RRN
CE
MAD
IR-MAD
ISFA

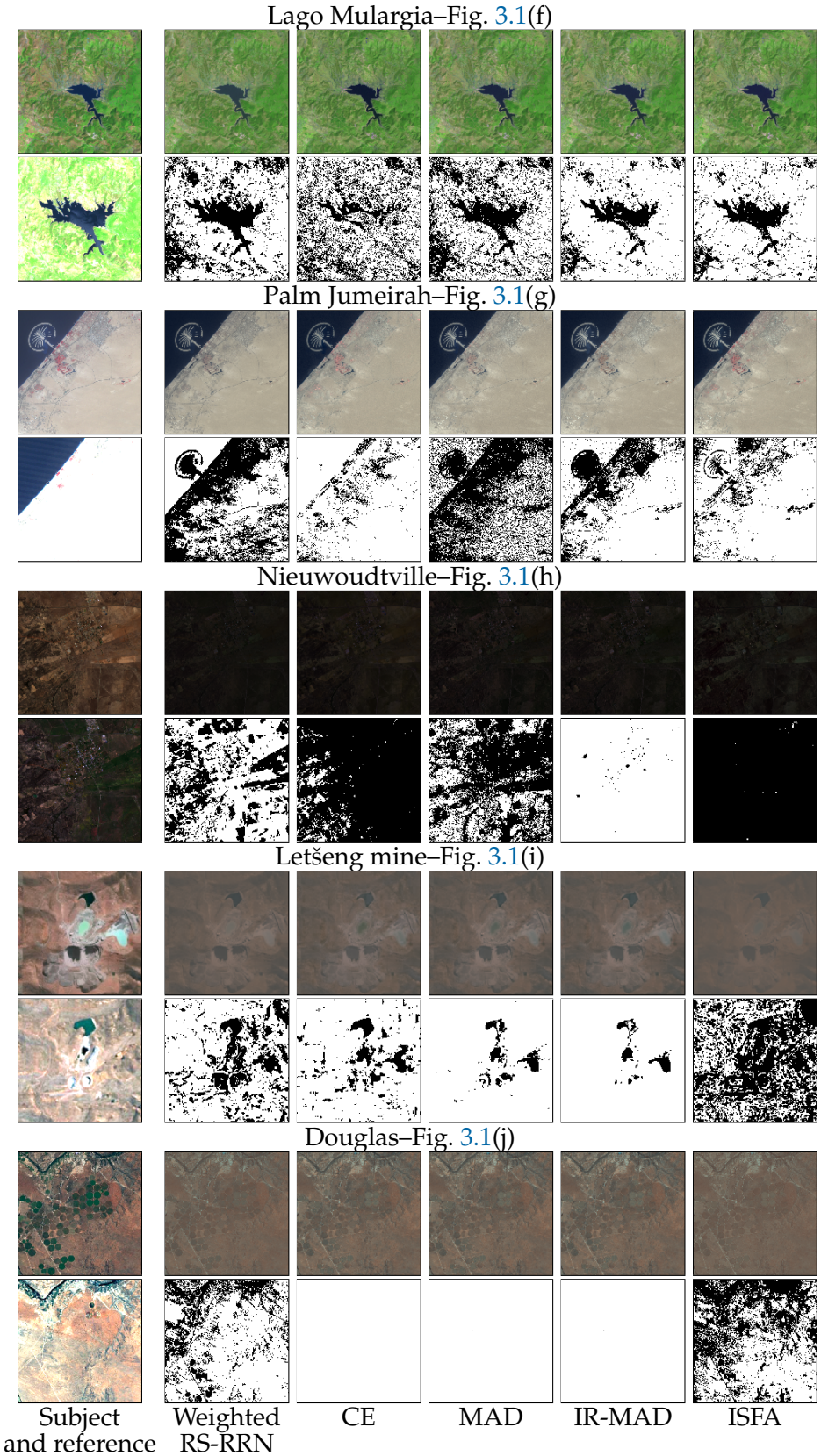


FIGURE 4.1: Normalised subject images (top row) and change maps (bottom row) produced by each radiometric normalisation algorithm

define suitable inlier cut-off thresholds. Iterative reweighting more distinctly separates inlier pixels from outliers in the MAD case, and key outliers are identified for image pair (c), although the control set still remains the full pixel set in the IR-MAD analysis for image pair (i).

4.3 Other RANSAC-based algorithms

Additional extensions to RANSAC were also considered for radiometric normalisation in the research. Weighted RANSAC is found to perform better than PROSAC, R-RANSAC or LO-RANSAC in terms of computational times and yielded structural similarity scores. These results have been excluded from the analysis, since these are also new methods which do not allow for time and structural similarity benchmarking.

The use of PROSAC, developed as an extension to RANSAC using non-random sampling, does not yield better results in the test cases used within this research. The advantages brought about by PROSAC in the favouring of better corresponding pixels are similarly achieved through the weighting scheme, where better pixels are pre-assigned higher weights, which increase their chances of being sampled. The fact that only $s = 2$ pixels are chosen at each iteration also diminishes the positive impact brought about by PROSAC, since it relies on a decreasing subset of the chosen pixels being sampled non-randomly.

R-RANSAC leverages a verification strategy based on Wald's theory of sequential decision making, to pre-emptively disregard samples with low likelihoods of yielding good correspondences. In the relative radiometric calibration case using only $s = 2$ pixels with a multilinear model, each model calculation requires minimal computing time, below the computing times of multiple Wald tests, which means R-RANSAC does not reduce overall computing times. Furthermore, the pre-weighting scheme radically decreases the probability of selecting poor samples, which further decreases the need for a Wald-test based filtering.

LO-RANSAC utilises the RANSAC methodology, but repeats the analysis in a subroutine within each iteration, by reperforming RANSAC on the inlier pixels identified under each hypothesis model. Because the minimal sample in this research is $s = 2$, and model calculations are not computationally expensive for the original random sampling method, the subroutine introduced by LO-RANSAC

unduly increases computing times of the overall routine. It is also found not to improve structural similarity or mean squared error results.

4.4 Summary

The weighted RS-RRN is found to perform favourably compared to the uniform RS-RRN and the SLIC RS-RRN algorithms in terms of computing times and structural similarity scores, and the three random sampling-based methods converge when the maximum number of samples is increased. The convergence of the weighted random sampling method is stronger than that of the other RS-RRN methods, while there is also a significant improvement over the computational times of the SLIC RS-RRN algorithm. The weighted RS-RRN algorithm is subsequently chosen as the algorithm to compare to the other radiometric normalisation methods.

The weighted RS-RRN is found to perform better or similarly to the MAD and CE algorithms in terms of structural similarity in all of the test cases, and significantly better than the MAD and CE algorithms in 6 and 5 cases respectively. In addition, it is only computationally more expensive than the CE algorithm for one of the data pairs. It is also found to perform significantly better in terms of the peak signal-to-noise ratio than the MAD algorithm in 9 cases, and significantly better than the CE algorithm in 8 cases.

The weighted RS-RRN also consistently achieves lower computing times than those of the IR-MAD and ISFA algorithms, while not demonstrating any significant sacrifice in the structural similarity scores for any of the image pair data cases. The increase in computing times for the weighted RS-RRN are also not as significant as the IR-MAD or ISFA when image sizes are larger or the number of spectral bands are increased. This makes the weighted RS-RRN algorithm suitable for use in the spectral calibration of multitemporal images.

Although several modifications to the RANSAC algorithm (such as PROSAC, LO-RANSAC, USAC) have been suggested in a more general context, these were found not to provide any computational or calibration advantage over the standard RANSAC algorithm when applied to radiometric normalisation.

Chapter 5

Conclusions and Future Work

5.1 Conclusions

Within this research, a random sampling relative radiometric normalisation (RSRRN) was developed, where relative radiometric normalisation was leveraged together with a random sampling mechanism to align multispectral images of the same area at different time points. The algorithm was extended to incorporate preweighting for pixel selection, with favourable computational and calibration results. The weighted algorithm was compared to the Covariance Equalisation, Multivariate Alteration Detection, Iteratively Reweighted Multivariate Alteration Detection and the Iterative Slow Feature Analysis algorithms in terms of their running times, SSIM scores and mean squared errors.

The Covariance Equalisation and Multivariate Alteration Detection algorithms showed fast computing times, even when image sizes or the number of spectral bands were increased. However, these algorithms showed the least favourable PSNR and SSIM scores, even after parameter optimisation. In some cases, these algorithms were not able show improvement over the full regression models.

Both of the iterative methods, namely the Iteratively Reweighted Multivariate Alteration Detection and the Iterative Slow Feature Analysis, showed favourable SSIM and PSNR scores, but demonstrated large computing times, especially when the number of spectral bands was increased. In one case, the Iteratively Reweighted Multivariate Alteration Detection algorithm was not able to improve on the similarity scores yielded by the full regression model.

The proposed random sampling-based iterative RRN method is found to generally perform better than the other RRN methods considered in this paper. The computing time of the proposed method is also generally less sensitive to image

sizes or the number of bands than the other methods, making the proposed method even more favourable when the image sizes or the number of bands are large. Furthermore, its parameters for thresholding and maximum number of iterations can be adaptively calibrated based on image characteristics, so it does not display other methods' sensitivity to parameter selection. Since only a small number of pixels are sampled at a time, the proposed method also does not necessarily require the loading of entire images into the memory as the other methods do, and could therefore handle the radiometric normalisation of very high resolution images. This verifies the tractability of random sampling for the radiometric calibration of co-registered images.

5.2 Future Work

Radiometric calibration of images with different resolutions or images covering differing but overlapping areas is not considered, but the proposed research could be extended in future to encompass a combination stitching and relative radiometric normalisation RANSAC algorithm to address this.

Preweighting of the Iteratively Reweighted MAD and the Iterative Slow Feature Analysis is also not considered further, although a comparison of IR-MAD, ISFA and RS-RRN results under similar initial weighting schemes would provide a suitable topic for future research.

The use of non-linear kernel-based mapping or neural network-based methods may also prove valuable in the relative radiometric normalisation of image pairs. These methods have not been considered, but provide an alternative to the linear mapping techniques used in this research, and comprise a suitable set of extensions to this research.

Lastly, since none of the considered algorithms utilise supervised learning, the identification and rejection of known outliers were not considered in this research. The testing of the capability of each model in the identification of known changed pixels or the incorporation of known values in the model calibration would provide useful further information on the tractability of the model in real-life applications.

Bibliography

[1] Radhakrishna Achanta et al. “SLIC superpixels compared to state-of-the-art superpixel methods”. In: *IEEE transactions on pattern analysis and machine intelligence* 34.11 (2012), pp. 2274–2282.

[2] Ondrej Chum and Jiri Matas. “Matching with PROSAC-progressive sample consensus”. In: *2005 IEEE computer society conference on computer vision and pattern recognition (CVPR'05)*. Vol. 1. IEEE. (2005), pp. 220–226.

[3] Ondřej Chum, Jiří Matas, and Josef Kittler. “Locally optimized RANSAC”. In: *Joint Pattern Recognition Symposium*. Springer. (2003), pp. 236–243.

[4] John C Clarke, S Carlsson, and Andrew Zisserman. “Detecting and Tracking Linear Features Efficiently.” In: *BMVC*. Citeseer. (1996), pp. 1–10.

[5] Martin A Fischler and Robert C Bolles. “Random sample consensus: a paradigm for model fitting with applications to image analysis and automated cartography”. In: *Commun. ACM* 24.6 (1981), pp. 381–395.

[6] Maoguo Gong et al. “Change Detection in Synthetic Aperture Radar Images Based on Deep Neural Networks”. In: *IEEE Transactions on Neural Networks and Learning Systems* 27.1 (2016), pp. 125–138. DOI: 10.1109/TNNLS.2015.2435783.

[7] Aleš Leonardis and Horst Bischof. “Robust recognition using eigenimages”. In: *Computer Vision and Image Understanding* 78.1 (2000), pp. 99–118.

[8] Jiri Matas and Ondrej Chum. “Randomized RANSAC with sequential probability ratio test”. In: *Tenth IEEE International Conference on Computer Vision (ICCV'05) Volume 1*. Vol. 2. IEEE. (2005), pp. 1727–1732.

[9] Philip F McLauchlan and Allan Jaenicke. “Image mosaicing using sequential bundle adjustment”. In: *Image and Vision computing* 20.9-10 (2002), pp. 751–759.

[10] A. A. Nielsen. "The Regularized Iteratively Reweighted MAD Method for Change Detection in Multi- and Hyperspectral Data". In: *IEEE Trans. Image Process.* 16.2 (Feb. 2007), pp. 463–478.

[11] A. A. Nielsen, K. Conradsen, and J. J. Simpson. "Multivariate Alteration Detection (MAD) and MAF Postprocessing in Multispectral, Bitemporal Image Data: New Approaches to Change Detection Studies". In: *Remote Sens. Environ.* 64.1 (1998), pp. 1–19.

[12] Philip Pritchett and Andrew Zisserman. "Wide baseline stereo matching". In: *Sixth International Conference on Computer Vision (IEEE Cat. No. 98CH36271)*. IEEE. (1998), pp. 754–760.

[13] Rahul Raguram et al. "USAC: a universal framework for random sample consensus". In: *IEEE transactions on pattern analysis and machine intelligence* 35.8 (2012), pp. 2022–2038.

[14] Frederik Schaffalitzky and Andrew Zisserman. "Viewpoint invariant texture matching and wide baseline stereo". In: *Proceedings Eighth IEEE International Conference on Computer Vision. ICCV 2001*. Vol. 2. IEEE. (2001), pp. 636–643.

[15] Alan P Schaum and Alan Stocker. "Hyperspectral Change Detection and Supervised Matched Filtering Based on Covariance Equalization". In: *Proc. SPIE*. Vol. 5425. (2004), pp. 77–90.

[16] John R Schott, Carl Salvaggio, and William J Volchok. "Radiometric scene normalization using pseudoinvariant features". In: *Remote Sens. Environ.* 26.1 (1988), pp. 1–16.

[17] Philip HS Torr and David W Murray. "Outlier detection and motion segmentation". In: *Sensor Fusion VI*. Vol. 2059. International Society for Optics and Photonics. (1993), pp. 432–443.

[18] Philip HS Torr, Andrew Zisserman, and Stephen J Maybank. "Robust detection of degenerate configurations while estimating the fundamental matrix". In: *Computer vision and image understanding* 71.3 (1998), pp. 312–333.

[19] Tinne Tuytelaars and Luc J Van Gool. "Wide Baseline Stereo Matching based on Local, Affinely Invariant Regions." In: *BMVC*. Vol. 412. (2000).

[20] A Wald. "Sequential Analysis. John Wiley & Sons, Inc". In: (1947).

[21] Zhou Wang et al. “Image quality assessment: from error visibility to structural similarity”. In: *IEEE Trans. Image Process.* 13.4 (2004), pp. 600–612.

[22] Junfeng Xu et al. “Combining iterative slow feature analysis and deep feature learning for change detection in high-resolution remote sensing images”. In: *Journal of Applied Remote Sensing* 13.2 (2019), p. 024506.

[23] Zhaohui Yin et al. “A Nonlinear Radiometric Normalization Model for Satellite Imgaes Time Series Based on Artificial Neural Networks and Greedy Algroithm”. In: *Remote Sensing* 13.5 (2021). ISSN: 2072-4292. DOI: 10.3390/rs13050933. URL: https://www.mdpi.com/2072-4292/13/5/933.

[24] Liangpei Zhang, Chen Wu, and Bo Du. “Automatic Radiometric Normalization for Multitemporal Remote Sensing Imagery with Iterative Slow Feature Analysis”. In: *IEEE Trans. Geosci. Remote. Sens.* 52.10 (2014), pp. 6141–6155.

[25] Lu Zhang et al. “Robust approach to the MAD change detection method”. In: *Proc. SPIE*. Vol. 5574. (2004), pp. 184 –193.